EurJIC
European Journal of Inorganic Chemistry

A Journal of ChemPubSoc Europe

Accepted Article

Title: Synthesis of BiOF/TiO2 heterostructures and their enhanced visible-light photocatalytic activity

Authors: Maryline NASR, Wenshi Huang, Carla Bittencourt, Dandan Cui, Ying Sun, Lei Wang, Nathalie Gaillard Caperaa, Yuping Ning, Ping Song, Pierre Bonnet, and Cong Wang

To be cited as: *Eur. J. Inorg. Chem.* 10.1002/ejic.201900970

Link to VoR: http://dx.doi.org/10.1002/ejic.201900970

WILEY-VCH

FULL PAPER WILEY-VCH

Synthesis of BiOF/TiO_2 heterostructures and their enhanced visible-light photocatalytic activity

Maryline Nasr,[a] Wenshi Huang,[b] Carla Bittencourt,[c] Dandan Cui,[b] Ying Sun,[b] Lei Wang,[b] Nathalie Gaillard Caperaa,[a] Yuping Ning,[b] Ping Song,[b] Pierre Bonnet,*[a] Cong Wang*[b]

Abstract: Novel BiOF/TiO_2 heterostructures with controlled amounts of BiOF and TiO_2 have been successfully synthesized via a simple solid-state sintering method. The structural, morphological and optical properties were analyzed using several characterization techniques. A shift of the TiO_2 absorption edge toward the visible region was observed. The optimal molar ratio of BiOF/TiO_2 was found to be (1:3) with a photodegradation percentage of 91.2% and it was 7 and 5 times more efficient than that of pure BiOF or TiO_2 nanopowder, respectively. BiOF/TiO_2 (1:3) heterojunction has showed high photodegradation stability for the Rh B photodegradation after three cycles. In the proposed photocatalytic mechanism, TiO_2 absorbed the visible light and carried out the photocatalytic reaction owing to the decrease of its band gap value due to the formation of oxygen vacancies, while BiOF played an important role in the charge separation process due to the intimate contact of the BiOF/TiO_2 heterojunction.

Introduction

In recent years, the serious water pollution was being addressed by the low cost and most efficient green technology, “photocatalysis”, which play an important role in solar energy conversion and degradation of organic pollutants.[1, 2] Among the numerous semiconductor photocatalysts, titanium dioxide (TiO_2) is the most used owing to its high chemical stability, low cost and nontoxicity.[3] Nevertheless, TiO_2 has a wide band gap energy (3.2eV), so it can only be excited by ultraviolet light with a wavelength < 388 nm which is equivalent to less than 7% of solar light.[4] However, the solar spectrum mostly consists of visible light (44%). Thus, the use of solar light as irradiation source for TiO_2 photocatalyst seems to be quite difficult. In addition, the high rate of the charge recombination in TiO_2 limits its photocatalytic activity efficiency.[5] Therefore, several strategies such as metal/non-metal doping,[6, 7] coupling with other semiconductor and heterostructure junctions have been investigated to overcome these limitations and enhance the photocatalytic activity of TiO_2 under visible light.[8] Among these strategies, the heterostructure design is a promising method to enhance the TiO_2 photocatalytic properties. Several studies have been devoted to design a heterojunction based on TiO_2 material such as g-C_3N_4/TiO_2, Ag-AgBr/TiO_2, BiOX (X=Cl, Br and I)/TiO_2…[4, 9-12] It was found that the close interfacial contact of the heterojunction promotes the transfer of photoinduced carriers from the TiO_2 surface to the other component which increase the life time of the charge carriers and consequently enhance the photocatalytic activity of TiO_2.[4, 11] In addition, it was reported that the design of these heterostructures increase the active surface area of TiO_2 and reduce its band gap energy which will improve its photocatalytic activity under visible light.[9] Much attention has been devoted recently to bismuth oxyhalides BiOX (X=Cl, Br, F and I) due to their high chemical stability and favorable photocatalytic performance under UV irradiation.[13] In particular, bismuth oxyfluoride (BiOF) exhibits a wide direct band gap estimated between 3.6 and 4.2 eV. The BiOF atomic structure is formed by layers of ($Bi_2O_2F_2$).[13] Recently, some studies have been reported on BiOF material [14, 15] but these studies remain not sufficient and not developed as for other BiOX compounds.[16]

To the best of our knowledge no studies have been reported on the bismuth oxyfluoride/titanium oxide (BiOF/TiO_2) photocatalyst. Therefore, in the present work we will report for the first time on the synthesis of BiOF/TiO_2 heterostructure photocayalst with the aim to enhance the photocatalytic performance of TiO_2 under visible light. Herein, BiOF/TiO_2 composites with different amounts of BiOF and TiO_2 were successfully synthesized via simple solid state sintering method. The structural, morphological and optical properties of the as-synthesized BiOF/TiO_2 heterostructures were analyzed using different characterization techniques. The main objectives of this work are to study the effect of BiOF on the photocatalytic properties of TiO_2, to report the optimum molar ratio BiOF/TiO_2 and to understand the photocinduced mechanism. The performance of the synthesized materials for the photodegradation of rhodamine B (Rh B) and methylene blue (MB) have been evaluated under visible light irradiation.

Results and Discussion

Figure 1-A shows XRD patterns of the different molar ratios of BiOF/TiO_2. The diffraction peaks were indexed with (*) for BiOF crystalline phase and (O) for TiO_2 anatase phase. All the identified peaks can be assigned to the tetragonal structure of BiOF and anatase phase of TiO_2. The sharp XRD diffraction peaks can be assigned to the (001), (101), (002), (110), (102), (003), (112), (200), (103), (211), (212) and (104) crystal planes of BiOF which correspond to 2θ = 14.28°, 27.90°, 28.85°, 33.87°, 37.68°, 43.76°, 45.10°, 48.68° 50.45°, 56.89°, 62.03° and 64.95° respectively.[17] The XRD diffraction peaks for pure anatase phase of TiO_2 were detected at 2θ = 26.35°, 48.15°, 54.05° and 55.28° corresponding to the (101), (200), (105) and (211) crystal planes, respectively.[18] Furthermore, no peaks related to metallic bismuth (Bi) or other crystalline phases and impurities were detected, confirming the heterostructure’s formation of the BiOF and TiO_2 pure phases.[17] This result will be confirmed later by Raman spectroscopy. In addition, it was

[a] Dr. M. Nasr, Dr. P. Bonnet, Mrs. Gaillard Caperaa
Institute of Chemistry of Clermont-Ferrand, Université Clermont Auvergne, Campus des Cezeaux, batiment chimie 5, 24 Avenue Blaise Pascal, 63178-AUBIERE Cedex, France
Email:pierre.m.bonnet@uca.fr
[b] Mr. W. Huang, Mr. D. Cui, Mr. Y. Sun, Mr. L. Wang, Mr. Y. Ning, Mr. P. Song, Dr. C. Wang
Center for Condensed Matter and Material Physics, Department of Physics, Beihang University, Beijing 100191, P.R.China
Email:congwang@buaa.edu.cn
[c] Mrs. C. Bittencourt
Chimie des Interactions Plasma-Surface (ChIPS), University of Mons, Place du Parc 22, 7000 Mons, Belgium

Supporting information for this article is given via a link at the end of the document

noted that the peak intensity corresponding to the (101) plane of TiO_2 anatase phase is increasing progressively with the increasing of TiO_2 amounts in BiOF/TiO_2 samples, while the peak intensity of BiOF is decreasing (Figure 1-A (d), (e) and (f)).

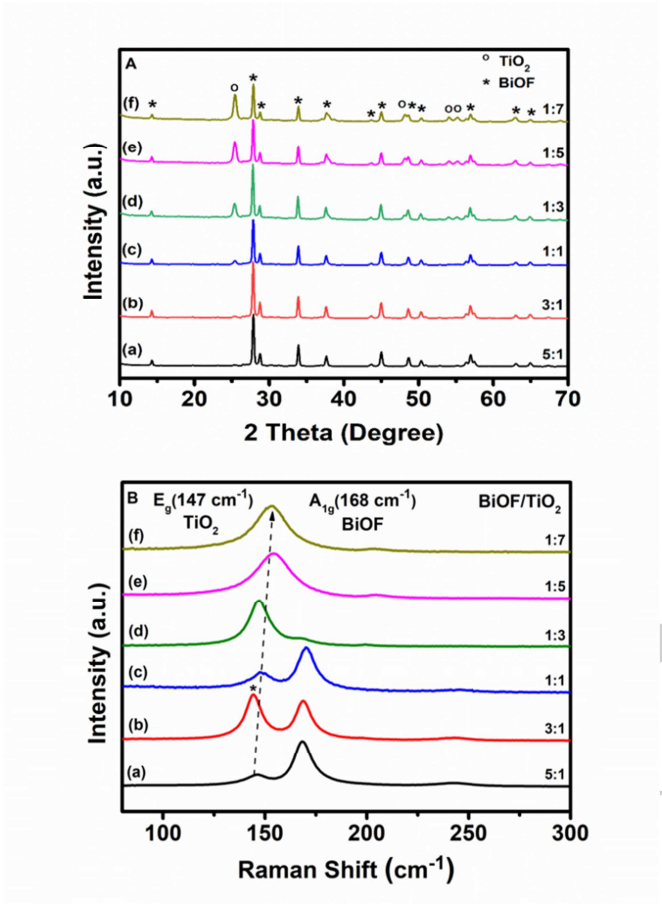

Figure 1. (A) XRD patterns and **(B)** Raman spectra of BiOF/TiO_2 with different molar ratios (a) 5:1 (black line), (b) 3:1 (red line), (c) 1:1 (blue line), (d) 1:3 (green line), (e) 1:5 (pink line) and (f)1:7 (brown line). **(A)** BiOF and TiO_2 crystalline phase are indexed with (*) and (O), respectively. **(B)** For the sample BiOF/TiO_2 with a molar ratio of (3:1) an increase of the TiO_2 peak intensity (indexed with *) was noticed despite the small amount of TiO_2 in the composite, this result can be explained by the fact that the laser beam has been focused on an area rich in TiO_2 nanoparticles.

Furthermore, the average crystal size of the BiOF/TiO_2 composites with different molar ratio of BiOF and TiO_2 was calculated using Scherrer-Debye equation:[19]

$$D = k\lambda/\beta\cos\theta \qquad \text{(Equation 2)}$$

where D is the average crystal size (nm), k is the shape factor constant (0.9), λ is the X-ray wavelength (0.154 nm), β is the full width at half maximum of the peak intensity (FWHM) and θ is the Bragg angle (degrees). The calculated results presented in Table 1 show a high grain fineness number of BiOF for all the samples as we can notice an increasing of TiO_2 average crystal size with the decreasing of the molar ratio of BiOF/TiO_2 (Table 1).

This increasing could be attributed to the grains sintering during the heat treatment under argon. In fact the dilution of TiO_2 by BiOF causes a decreasing of TiO_2 crystallite size and vice versa.[20] The successful formation of BiOF/TiO_2 composites was further confirmed by Raman spectroscopy as shown in Figure 1-B. For all the BiOF/TiO_2 prepared samples 2 peaks were detected in Raman spectra, a first peak located at 147 cm^{-1} and corresponding to the E_g vibrational mode of TiO_2 anatase phase and a second peak located at 168 cm^{-1} and can be assigned to the A_{1g} vibrational mode of BiOF.[5, 17] As shown in Figure 1-B, the main TiO_2 peak was shifted from the initial position with the increasing of TiO_2 amount in the BiOF/TiO_2 composites. This significant shift varied between 2 and 6 cm^{-1} and could be attributed to the defects and oxygen vacancies' formation in the TiO_2 lattice.[21] In addition, it could be observed that with the increasing of TiO_2 amounts the intensity of TiO_2 Raman's peaks increased while the intensity of BiOF Raman's peaks decreased (Figure 1-B, (a) and (c) to (f)). Moreover, no peak related to metallic bismuth (Bi) at ~ 96 cm^{-1} was detected by Raman, which confirmed that no or only few oxygen vacancies' and defects were formed in BiOF lattice.[17] This result is in a good agreement with the XRD analysis and confirming the heterostructure's formation of the two pure phases of BiOF and TiO_2.

Table 1. Grain size of BiOF and TiO_2 in BiOF/TiO_2 heterostructures.

Molar ratio	(5:1)	(3:1)	(1:1)	(1:3)	(1:5)	(1:7)
BiOF	45	45	45	52	48	48
TiO_2	19	19	28	29	30	30

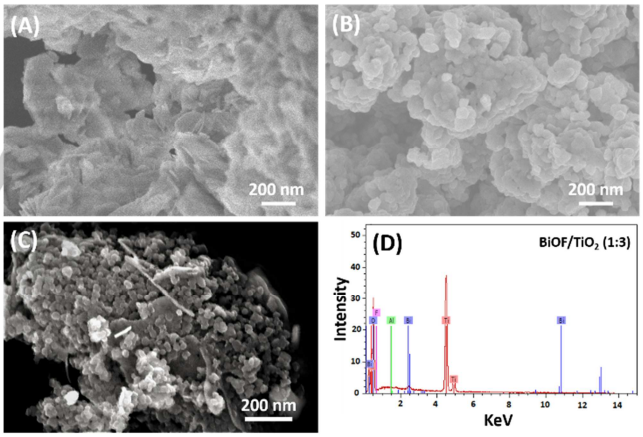

Figure 2: Scanning electron microscope images of **(A)** BiOF plates, **(B)** TiO_2 nanoparticles, **(C)** BiOF/TiO_2 (1:3) heterostructure and **(D)** EDX data showing the composition BiOF/TiO_2 (1:3) heterostructure, the peak corresponding to Al element in the EDX data is due to the sample holder which is composed from aluminum material.

All the samples were analyzed by the different characterization techniques; however the analyses of BiOF/TiO_2 (1:3) are given as an example. The morphology of the samples was investigated by scanning electron microscope and to confirm the formation of BiOF/TiO_2 composites heterojunction. The average

diameters and the thickness were measured using image analysis software (Image J1.29X). Figure 2-(A) shows a single phase of BiOF which is plate-like with a smooth surface, the thickness and the average diameter of these plates are around 15 ± 1 nm and 250 ± 10, respectively. TiO_2 nanoparticles are shown in Figure 2-(B), a highly interconnected network with randomly oriented nanoparticles is clearly observed. The average diameter of TiO_2 nanoparticles was measured from Figure 2-(B) and it was found to be around 116 ± 5 nm. BiOF/TiO_2 sample with the molar ratio of 1:3 is shown in Figure 2-(C). The deposition of TiO_2 nanoparticles on the entire surface of BiOF nanoplates revealed the intimate contact between the two materials (BiOF and TiO_2) as well the formation of BiOF/TiO_2 heterojunction. The presence of different elements Bi, O, F and Ti was detected from the energy dispersive X-ray spectrum (EDX) for the BiOF/TiO_2 (1:3) as shown in Figure 2-(D), no other elements were detected in the spectrum confirming that there is no impurity or contamination in the prepared sample. It is worth to note that the peak corresponding to Al element in the EDX data is due to the sample holder which is composed from aluminum material Elemental mapping images for BiOF/TiO_2 (1:3) composite are shown in Figure S1 (supporting information). We can clearly observe that Ti, Bi, O and F elements are distributed homogeneously over the entire area of the BiOF/TiO_2 sample. The XPS analysis confirms that the sample is mainly composed of Bi, O, F, Ti (Figure 3-A). The presence of carbon in the spectrum can be associated with adventitious carbon contamination from ambient exposure. A close inspection of the Ti 2p XPS and the Bi 4f core level spectra (Figure 3-B and C) indicates that the Ti and Bi atoms have mainly the oxidation state +4 and +3, respectively.[22, 23] The Ti 2p peak was reproduced using a Shirley background and 2 doublets, a high intensity one with the component $2p_{3/2}$ at 458.5eV and a low-intensity doublet shifted to lower binding energy by 2.3 eV, respectively. They can be associated to photoelectrons emitted from Ti atoms with oxidation state +4 and +3 respectively (Figure 3-B). As shown in Figure 3-C, two main peaks appeared at 159.1 and 164.5 eV and correspond to Bi $4f_{7/2}$ and Bi $4f_{5/2}$, respectively. These peaks are assigned to the characteristic peaks of Bi^{3+} in BiOF. Moreover, two weak peaks at 157 and 162.2 eV assigned to Bi^0 were observed demonstrating that only a small amount of Bi^{3+} was reduced to Bi^0 (metallic) in BiOF.[24]The oxygen 1s XPS spectrum presented in Figure3-D shows two components, the first one at 530.4 eV and the second one at higher binding energy, they have been associated to photoelectrons emitted from oxygen atoms in TiO_2[25] and in Bi-O bonding,[26] respectively. Due to the small amount of vacancies, it is difficult to identify a single component that can be associated to photoemission from oxygen atoms near vacancies. It is reported that for TiO_2 this component would be centered in the range of 531.6-532.0 eV,[27, 28] thus being overlapped by the component associated to Bi-O. At the same time, as presented above, no peaks related to the metallic Bi were detected by XRD and Raman analyses which confirm the small amount of Bi^0/oxygen vacancies in BiOF. Surface area of BiOF/TiO_2 (1:3) nanocomposite was calculated using the Brunauer–Emmet–Teller method (BET) and it was found to be 53.60 m^2/g which is a large surface area and could offer more active adsorption sites and consequently could enhance the BiOF/TiO_2 photocatalytic activity.

Transmission electron microscopy was furthermore performed on the as-synthesized TiO_2 and BiOF/TiO_2 photocatalysts to confirm the formation of BiOF/TiO_2 heterojunction. The granular aspect and the uniform particle size of BiOF/TiO_2 (1:3) nanocomposite are clearly observed in Figure 4-(A). The nanoparticles have rather rounded and slightly elongated shapes with sizes around 20 nm. The TEM image of BiOF/TiO_2 (1:3) composite in Figure 4-(B) confirms the good crystalline structure of BiOF and TiO_2 which is in a good agreement with XRD results presented above. As shown in Figure 4-(C and D), the *d* spaces of TiO_2 and BiOF were found to be 0.320 nm and 0.410 nm, corresponding to the (110) plane of anatase phase of TiO_2 and the (111) plane of tetragonal phase of BiOF, respectively.[29, 30] In addition, from Figure 4-B we can clearly see the intimate contact between the two crystalline structures of BiOF and TiO_2 nanomaterials confirming the formation of heterojunction between BiOF nanoplates and TiO_2 nanoparticles. As conclusion, this close interfacial contact of the heterojunction will probably promote the transfer of the charge carriers from TiO_2 to BiOF surface which will reduce the charge recombination and therefore enhance the photocatalytic activity as it will be confirmed later in the photocatalytic section.[31]

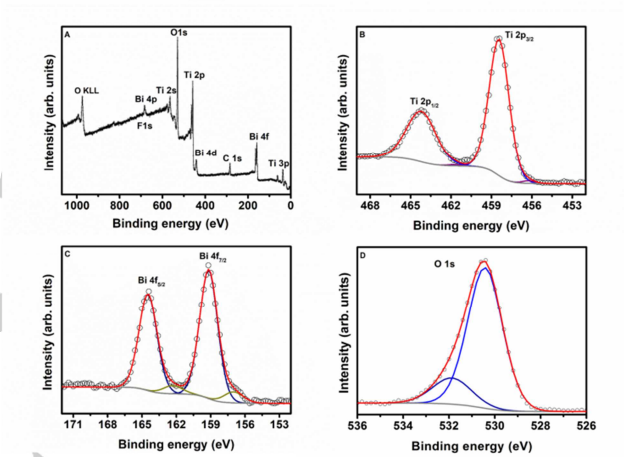

Figure 3. XPS spectra of **(A)** BiOF/TiO_2 (1:3), **(B)** Ti 2p peaks of TiO_2, **(C)** Bi 4f peaks of BiOF and **(D)** O 1s peaks of TiO_2 and BiOF.

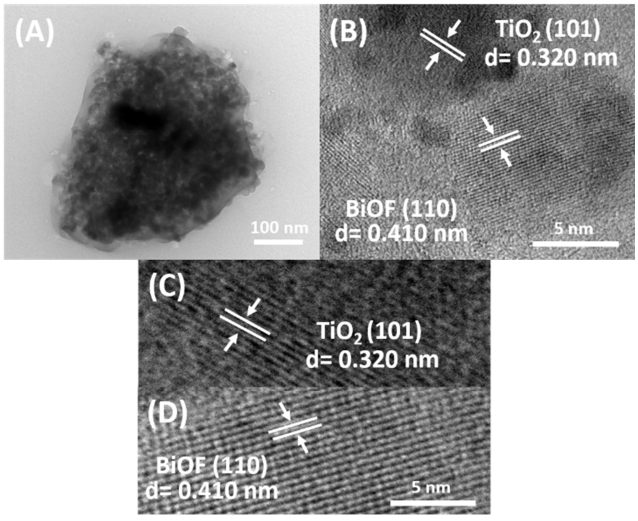

Figure 4. TEM images of **(A-B)** BiOF/TiO_2 (1:3), **(C)** partial enlarged image of TiO_2 region in **(B)** and **(D)** partial enlarged image of BiOF region in **(B)**.

The successful formation of pure BiOF/TiO_2 composite heterojunctions with appropriated interfaces was confirmed by XRD, Raman, SEM, TEM, EDX and XPS analyzes. To study the influence of BiOF on the optical properties of TiO_2 nanoparticles the UV-Visible diffuse reflectance was recorded for TiO_2, BiOF and BiOF/TiO_2 (1:3) powders as shown in Figure 5-A. The Tauc plot method was used to determine the semiconductor optical band gap using the following formula:[32]

$$(\alpha h\nu)^{1/2} \sim (h\nu - E_g) \qquad \text{(Equation 3)}$$

where α, hv and E_g represent the absorption coefficient, photon energy and band gap, respectively. The band gap values (E_g) correspond to the intersection of the linear part of the curve with hv-axis as shown in Figure 5-B. The band gap and the absorbance edge for the pure TiO_2 and pure BiOF powders were found to be (3.18 eV; 390 nm) and (3.67 eV; 338 nm), respectively, which are close to the values reported in the literature.[33, 34] As shown in Figure 5-A, BiOF/TiO_2 (1:3) heterostructure exhibits stronger absorption intensity in the visible light range due to the creation of oxygen vacancies during the heat treatment, therefore, a stronger photocatalytic activity in the visible range, compared with TiO_2 and BiOF. Moreover, a red-shift of the absorption edge (410 nm) was observed compared with the pure BiOF and pure TiO_2. This red-shift resulted in a decrease of the band gap value from 3.18 eV to 3.02 eV and this decrease can be attributed to the oxygen vacancies and defects' mainly formed in the TiO_2 lattice as confirmed by the structural analyzes presented above.[35] According to the literature, the formation of oxygen vacancies during the synthesis of materials can be explained by the heat treatment under argon atmosphere at 350°C which introduces surface defects in the form of oxygen vacancies in TiO_2 structure.[36, 37] This is confirmed by electron spin resonance spectroscopy analysis (ESR) as shown in Figure S2 (supporting information). A small amount of oxygen vacancies can also be presented in BiOF lattice as already shown by XPS. Therefore, the decrease of the band gap value of BiOF/TiO_2 (1:3) heterojunction compared with pure TiO_2 will possibly lead to an increase of the photocatalytic efficiency under visible-light irradiation.[38] Photocurrent characterization was conducted on a CHI650D electrochemical workstation with a standard three-electrode system. A platinum wire acted as counter electrode, and a standard saturated calomel electrode (SCE) in saturated KCl acted as reference electrode, 0.1M Na_2SO_4 was used as electrolyte. The prepared sample was coated on the fluorine doped tin oxide glass, which was used as the working electrode. As shown in Figure 5-C, all the electrodes were prompt in generating photocurrent with a reproducible response to on/off cycles. As results, the BiOF/TiO_2 (1:3) electrode exhibits a higher photocurrent density (~1.10^{-6} μA/cm^{-2}) compared with the pure BiOF (~1.10^{-7} μA/cm^{-2}) or TiO_2 (~5.10^{-7} μA/cm^{-2}) indicating the efficient photoinduced charge separation in BiOF/TiO_2 (1:3) heterojunction. Therefore, this heterojunction will probably presents an enhanced photocatalytic activity compared with pure TiO_2 or BiOF.[39]

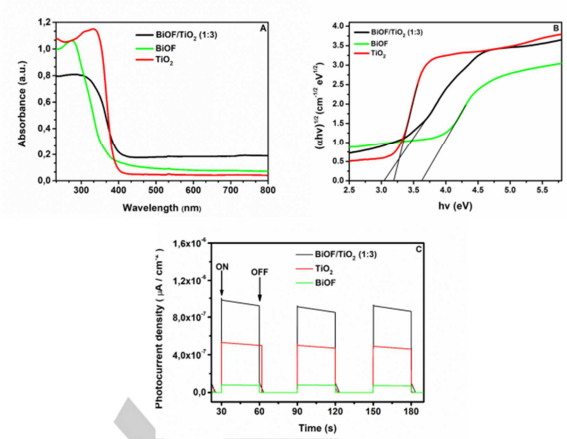

Figure 5: (A) UV-Visible diffuse reflectance spectra, **(B)** and **(C)** Visible light excited photocurrent of TiO_2 (red line), BiOF (green line) and BiOF/TiO_2 (1:3) (black line).

It is worth noting that our work is focused on the material preparation and not on the investigation of the pollutant degradation mechanism. According to the literature, the photodegradation pathway of pollutants is based on the excitation of the semiconductor which will lead to the formation of electron-hole pairs that participate in the redox reactions to degrade or to reduce the adsorbed molecules such as organic pollutants (Rh B, MB…).[2] The photodegradation process could be described by the following equations:[40]

$$\text{Semiconductor} + h\nu \rightarrow h^+ + e^- \qquad \text{(Equation 4)}$$

$$H_2O + h^+_{\text{(valence band)}} \rightarrow HO^\bullet + H^+ \qquad \text{(Equation 5)}$$

$$h^+_{\text{(valence band)}} + \text{pollutant} \rightarrow \text{pollutant}^+ \qquad \text{(Equation 6)}$$

$$HO^\bullet + \text{pollutant} \rightarrow H_2O + CO_2 \qquad \text{(Equation 7)}$$

$$h^+ + e^- \rightarrow \text{heat} \qquad \text{(Equation 8)}$$

The photocatalytic activity of the as-prepared samples has been evaluated under visible light using Rh B as a model pollutant (Figure 6-A). After 90 minutes of light irradiation, the photodegradation percentage of Rh B was up to 73.9%, 84.9% , 91.2% , 89.1% , 86.9% and 70.7% for BiOF/TiO_2 samples with a molar ratio of (1:7), (1:5), (1:3), (1:1), (3:1) and (5:1), respectively. As clearly seen, the BiOF/TiO_2 (1:3) exhibits the highest photocatalytic activity among the other heterostructures. As shown in Figure 6-B, the blank test (without adding a photocatalyst) indicates that Rh B is stable and difficult to be photodegraded under visible light during 90 min. For comparison with the BiOF/TiO_2 (1:3) heterojunction, the photocatalytic activity of pure TiO_2, pure BiOF and a simple mixture of BiOF and TiO_2 (1:3) has been evaluated under the same experimental conditions. After illumination of 90 min, the percentage of Rh B removal reaches 40.2%, 28.5%, 32.5% and 91.2% for TiO_2, BiOF, simple mixture of BiOF and TiO_2 (1:3) and BiOF/TiO_2 (1:3) heterojunction, respectively (Figure 6-B). As results, the BiOF/TiO_2 heterojunctions with different molar ratios presents a greater photocatalytic activity compared with pure TiO_2 and pure BiOF nanomaterials. The enhancement of the photocatalytic efficiency under visible light is attributed to the following

reasons: (I) the close interfacial contact of the heterojunction, which promotes the transfer of charge between BiOF and TiO_2 surface and reduce the charge recombination, thus more electrons will be available to take part in the photodegradation process,[41, 42] (II) the decrease of the BiOF/TiO_2 band gap due to the defects and oxygen vacancies' formation in TiO_2 and BiOF lattices,[17, 35] and (III) a good matching of BiOF and TiO_2 energy levels due to the oxygen vacancies' states.[43] Moreover, the (1:3) represents the optimal ratio for BiOF/TiO_2 with the highest photocatalytic activity (91.2%). Therefore, the use of an excessive amount of TiO_2 or BiOF will cause particle's aggregation which will reduce the light absorption on the surface and promotes the charge's recombination by increasing the collision between the photogenerated electrons and holes.[44, 45] Thus, the use of an excessive amount of TiO_2 or BiOF will lead to a decrease of the photocatalytic efficiency as it was confirmed in the present work (Figure 6 A-B). Since TiO_2 nanoparticles are on the surface of BiOF plates, the amount of TiO_2 should be predominant, but not in excess, in order to absorb the maximum of light and carried out the photocatalytic reaction. At the same time the amount of BiOF should be sufficient in order to be in an intimate contact with TiO_2 and to ensure the charges' separation and hence, increase the photocatalytic efficiency. Therefore, the BiOF/TiO_2 (1:3) composition presents the optimal ratio of BiOF and TiO_2 for the photocatalytic activity under visible light.

The kinetics of the photodegradation' curves were analyzed and the obtained results were presented in Figure 6-C. The photodegradation reactions followed a Langmuir– Hinshelwood first order kinetics model, as described by equation (9):[46]

$$\ln (C_0/C) = kKt = k_a t \qquad \text{(Equation 9)}$$

where C_0 corresponds to the initial concentration of Rh B solutions , C is the concentration of Rh B solution at time t, t is the irradiation time, k is the reaction rate constant (mg (L min)$^{-1}$), K is Rh B adsorption coefficient (mg L^{-1}) and k_a corresponds to the apparent first-order rate constant (min^{-1}). The obtained k_a values from the linear dependence between ln(C_0/C) and time are reported in Figure 6-C. The apparent rate constant value of all BiOF/TiO_2 heterojunctions is higher than that of pure BiOF and TiO_2 powder. Moreover, compared with other heterojunctions, BiOF/TiO_2 with the optimal ratio of (1:3) showed the highest photocatalytic activity under visible light, which is represented by the highest k_a value. The rate constant exhibits a maximum of 0.0273 min^{-1} for BiOF/TiO_2 (1:3), which is around 7 and 5 times higher than that of BiOF and TiO_2, respectively. Therefore, the heterojunction design between BiOF and TiO_2 greatly improves the photocatalytic activity under visible light. To investigate the potential reusability of these materials for the photocatalytic decomposition of Rh B under visible light, the photodegradation test has been repeated for three cycles under the same conditions and using BiOF/TiO_2 with the optimal ratio (1:3) as photocatalyst. After each cycle, the photcatalyst was separated from the solution by centrifugation to be used in the next cycle. It is worth noting that even after several photocatalytic cycles, the characteristic diffractions peaks of BiOF/TiO_2 (1:3) remains unchanged compared with the XRD pattern of BiOF/TiO_2 (1:3) before photocatalysis (Figure S3, supporting information). As shown in Figure 6-D, BiOF/TiO_2 (1:3) heterostructure shows a high stability for the photodegradation of Rh B with a percentage of 91.2%, 90.5% and 87.3% for the first, second and third cycle, respectively. A slight decrease of the photocatalytic efficiency was noted and could be due to the loss of photocatalyst during the centrifugation process.[47]The improvement of photocatalyst recovery at the end of degradation process may be improved, in particular by adding a small amount of magnetic material such as Fe_3O_4[48] or by depositing it on a support.[49]

In order to examine the photocatalytic capacity of the nanomaterial, the photodegradation activity was also analyzed using another dye, methylene blue (MB), and under the same experimental conditions used for Rh B. The BiOF/TiO_2 sample with the optimal ratio (1:3) has been employed as photocatalyst. The results in Figure 7 indicated that MB was stable and difficult to be photodegraded under visible light in the absence of photocatalyst. The BiOF/TiO_2 heterojunction was able to photodegrade MB up to 60% after 90 minutes compare to 43.7% and 27.1% for pure TiO_2 and BiOF, respectively. Therefore, the BiOF/TiO_2 (1:3) heterojunction exhibits an enhanced photocatalytic activity and stability compared with pure TiO_2, moreover this composite is able to photodegrade multiple dyes under visible light.

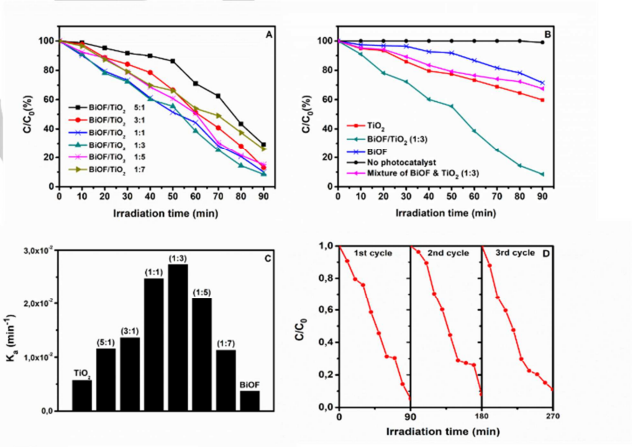

Figure 6: (A-B) Photocatalytic degradation of Rh B solution in the presence of TiO_2, BiOF and BiOF/TiO_2 with different molar ratios under visible light irradiation, **(C)** Apparent rate constants for the photodecomposition of RhB over BiOF, TiO_2, BiOF/TiO_2 heterostructures **(D)** Photocatalytic stability of BiOF/TiO_2 (1:3) in three repeated cycles for Rh B photocatalytic degradation under visible light irradiation.

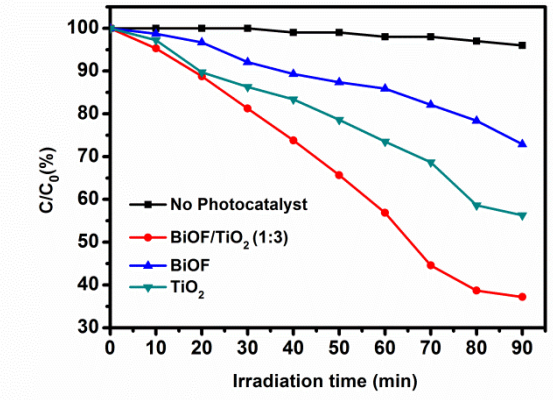

Figure 7: Photocatalytic degradation of methylene blue without photocatalyst (black line) and in the presence of photocatalyst: BiOF (blue line), TiO_2 (green line), BiOF/TiO_2 (1:3) (red line) under visible light irradiation.

In order to investigate the photo-induced carriers transfer route, the relative conduction band (CB) and valence band (VB) potentials of BiOF and TiO_2 were calculated using the following formulas:[4]

$$E_{VB} = \chi - E^e + \frac{1}{2}E_g \qquad \text{(Equation 10)}$$

$$E_{CB} = E_{VB} - E_g \qquad \text{(Equation 11)}$$

Where E_{VB} is the valence band (VB), χ is the absolute electronegativity and corresponds to the geometric mean of the absolute electronegativity of the constituents atoms; E^e is the energy of free electrons on the hydrogen scale *ca.* 4.5 eV and E_g corresponds to the band gap energy of the semiconductor. The band gap energies of BiOF and TiO_2 were calculated to be 3.66 and 3.18 eV, respectively. After calculation, the conduction band bottom and valence band positions (E_{CB} / E_{VB}) of the BiOF and TiO_2 were found to be 0.20/ 3.86 eV and -0.28/2.90 eV, respectively. It is well known that the key factor of an efficient photocatalytic activity is the charge separation at the interfaces of photocatalysts.[43] Therefore a proposed mechanism for the photogenerated charge separation and migration process in BiOF/TiO_2 heterostructured under visible-light irradiation is shown in Figure 8. The conduction band edge potential of TiO_2 (-0.28 eV) is more negative than that of BiOF (0.20 eV) which means that the photogenerated electrons on TiO_2 surface migrate easily to BiOF due to the close interfacial contact of the BiOF/TiO_2 heterojunction. Once transported to the surface of BiOF, these electrons will react with O_2 to form $O_2^{\cdot-}$ radicals. Moreover, the photogenerated holes in TiO_2 will oxidize the organic pollutant to H_2O or other inorganic molecules. This efficient migration process prevents the recombination of charge and hence improves the photocatalytic activity.[50,51] As results, TiO_2 absorbed the visible light and carried out the photocatalytic reaction owing to the decrease of its band gap value from 3.18 to 3.02 eV due to the oxygen vacancies' formation, while BiOF played an important role in the charge separation process due to the intimate contact of the BiOF/TiO_2 heterojunction. Few oxygen vacancies in BiOF could also participate to the optical absorption.

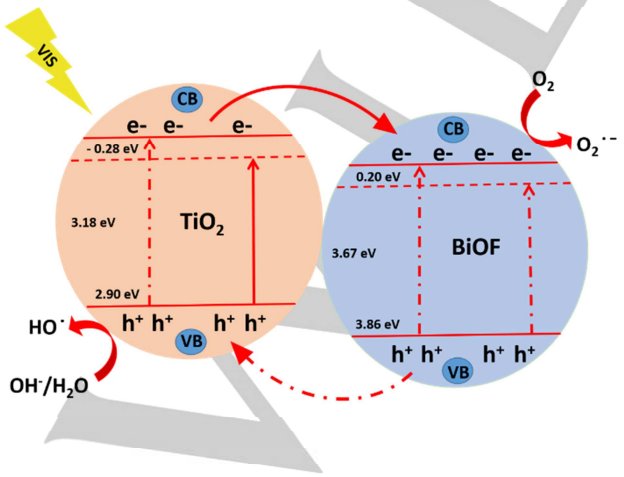

Figure 8: Proposed mechanism for the photogenerated charge separation and migration process in BiOF/TiO_2 heterostructured under visible-light irradiation. BiOF could be excited and participates to the photodegradation process (indexed by dashed arrows) only under UV light irradiation.

Conclusions

In summary, the novel BiOF/TiO_2 heterostructure with different molar ratio of BiOF and TiO_2 were successfully elaborated via simple solid state sintering method followed by a heat treatment at 350°C under argon atmosphere. The good crystalline phase of BiOF and TiO_2 and the formation of BiOF/TiO_2 heterostructures were confirmed by Raman and XRD analyzes. The chemical composition and the intimate contact between the two phases of BiOF and TiO_2 were revealed by XPS, EDX, SEM and TEM characterizations. The red shift of the absorbance edge and the decrease of the TiO_2 band gap value from 3.18 to 3.02 eV for the BiOF/TiO_2 (1:3) sample were confirmed by diffuse reflectance analysis. All the synthesized BiOF/TiO_2 heterostructures have presented an enhanced photocatalytic activity for the photodegradation of Rh B under visible light compared with pure TiO_2 or BiOF. The optimal molar ratio of (BiOF/TiO_2) was found to be (1:3) with a photodegradation percentage of 91.2% and it was 7 and 5 times more efficient than that of BiOF and TiO_2, respectively. In addition, the photocatalytic repeatability tests confirmed the long-term stability of BiOF/TiO_2 (1:3) heterojunction for Rh B photodegradation after three cycles. The optimal ratio (1:3) of BiOF and TiO_2 results from a good matching between TiO_2 and BiOF amounts where TiO_2 is predominant and absorbs the maximum of light and at the same time the BiOF amount is sufficient to be in an intimate contact with TiO_2 and to ensure the charges' separation and hence, increase the photocatalytic efficiency under visible light. The enhanced visible-light photocatalytic activity of BiOF/TiO_2 heterostructure was attributed to the following reasons: (I) the red-shift of the absorption edge due to the formation of oxygen vacancies mainly in TiO_2 lattice, (II) the good matching of BiOF and TiO_2 energy levels due to the oxygen vacancies' states and (III) the close interfacial contact between BiOF and TiO_2 nanomaterials, which reduces the charge's recombination and hence, increase the photocatalytic activity of BiOF/TiO_2 heterostructure under visible light. In conclusion, the BiOF/TiO_2 heterostructure is able to enhance the efficiency of the photocatalytic process in a simple manner and could be used as photocatalyst in the photodegradation of different molecules.

Experimental Section

Materials

Titanium (IV) oxide, anatase nanopowder (99.7%) with a particle size < 25 nm and Hydrofluoric acid solution (40%) were purchased from Sigma Aldrich. Bismuth (III) oxide (99.9%-Bi) was obtained from Strem Chamicals. All chemicals were used without any further purification.

Table 2: BiOF/TiO_2 nanocomposites prepared with different molar ratios of BiOF and TiO_2.

Sample Name	Molar Ratio of Bi:Ti
BiOF/TiO_2 (5:1)	5:1
BiOF/TiO_2 (3:1)	3:1
BiOF/TiO_2 (1:1)	1:1
BiOF/TiO_2 (1:3)	1:3
BiOF/TiO_2 (1:5)	1:5
BiOF/TiO_2 (1:7)	1 :7

Synthesis of BiOF/TiO_2 nanocomposite heterostructure

BiF_3 nanoparticles were synthesized in our laboratory by direct reaction between Bi_2O_3 and HF (aq) at 70°C in a Teflon beaker. The precipitate obtained through HF was removed by evaporation under a hood and as a final product we get BiF_3 powder. BiOF powder was obtained by a solid state sintering method in air using the synthesized BiF_3 nanoparticles and the commercial Bi_2O_3 powder with a molar ratio of BiF_3/Bi_2O_3 = 1:1. Then the mixture was heated at 425°C for 12 hours under argon atmosphere in order to obtain BiOF nanoparticles. BiOF/TiO_2 heterostructures with different molar ratios of BiOF and TiO_2 were also elaborated via a solid state sintering method. Therefore, different amounts of the synthesized BiOF and the commercial TiO_2 nanoparticles were mixed and grinded for 30 minutes. Then, the different mixtures of BiOF/TiO_2 were calcined at 350°C for 5 hours under argon atmosphere. The as-synthesized samples were labeled according to their molar ratios (BiOF/TiO_2) and are listed in Table 2. Pure BiOF and TiO_2 nanomaterials were calcined under the same conditions to serve as references in the photocatalytic section.

Chemical and Physical Characterizations

The structure of the samples were characterized by X-ray diffraction (XRD) using a PANAlytical Xpert-PRO diffractometer (Cu-radiation, λ = 1.5406 Å) and Raman spectroscopy using a Jobin Yvon T64000 spectrometer (λ = 514.5 nm; 2.41 eV) in a confocal microscopy mode in air at room temperature. Energy dispersive X-ray photoelectron spectroscopy analysis (EDX) was taken with a Hitachi S3500. The surface area was determined from nitrogen adsorption-desorption isotherms at liquid nitrogen temperature using the Micromeritics ASAP 2010 system (outgassing conditions: 200°C-12 h). X-ray photoelectron spectroscopy (XPS) was performed using a Versaprobe PHI 5000 spectrometer from Physical Electronics, equipped with a monochromatic Al Kα X-ray source. The base pressure at the analysis chamber was 10^{-9} mbar. The sample was mounted on double-sided conductive tape suitable for vacuum. The X-ray photoelectron spectra were collected at a take-off angle of 45° with respect to the electron energy analyzer and the spot size was 200 µm. The overall energy resolution was 0.5 eV. The analysis of the XPS spectra was implemented using the CASA XPS software. The morphology and the size distribution of the prepared nanomaterials were analyzed by scanning electron microscopy (SEM, Hitachi S3500) and transmission electron microscopy (TEM, Hitachi H-700). The UV-VIS absorbance spectra were recorded by a U-3010 UV-VIS spectroscopic spectrophotometer. The photocurrent density was measured using a CHI650D electrochemical workstation with a standard three-electrode system.

2.4. Photocatalytic activity

Rhodamine B (Rh B) and Methylene Blue (MB) were employed as organic pollutants' references to evaluate the photocatalytic activity of BiOF/TiO_2 composites under a 500W Xe lamp with a 420 nm cut off filter. The experiments were carried out in a homemade reactor with a cooling water system in order to keep the reaction's temperature constant at 25 ± 0.2°C. The photodegradation reactions were carried out in separates beaker containing a suspension of 20 mg of photocatalysts and 40 mL of MB or Rh B solution (10 mg/L). The suspensions were firstly stirred for 2 hours in dark to reach the adsorption/desorption equilibrium. The distance between the lamp and the dye solution was maintained at 10 cm. After light irradiation, every 10 minutes 2 mL of each solution was taken out and centrifuged at 6000 rpm for 2 minutes in the darkness. The centrifuged solutions were analyzed with a UV/VIS spectrometer to study the decrease in dyes' concentration over time during light irradiation. The absorbance of the solution was measured at 664 and 554 nm for Rh B and MB, respectively. The photocatalytic degradation efficiency has been calculated using equation 1:[32]

$$\text{Degradation efficiency (\%)} = (C_0 - C)/C_0 \times 100 \qquad \text{(Equation 1)}$$

Where C_0 and C are the initial and final dye's concentration, respectively.

Acknowledgments

This work was supported by NSFC (No.51572010, 51502010), Aeronautical Science Foundation of China (2014ZF51067), State Key Lab of Advance Metals and Materials (2014-ZD03) and Fundamental Research Funds for the Central Universities (Grand No. YWF-16-JCTD-B-03). The authors would like to thank Miss Maimonatou Mar and Mr. Lawrence Frezet's help.

Keywords: Heterojunction • Photocatalysts • TiO_2 • BiOF • visible-light photocatalysis •

[1] Y. Zhang, M. Sivakumar, S. Yang, K. Enever and M. Ramezanianpour, *Desalination*. **2018**, *428*, 116-145.
[2] M. Nasr, C. Eid, R. Habchi, P. Miele and M. Bechelany, *ChemSusChem*. **2018**, *11*, 3023-3047.
[3] M. Nasr, A. A. Chaaya, N. Abboud, M. Bechelany, R. Viter, C. Eid, A. Khoury and P. Miele, *Superlattices Microstruct.* **2015**, *77*, 18-24.
[4] D. Sánchez-Rodríguez, M. G. M. Medrano, H. Remita and V. Escobar-Barrios, *J. Environ. Chem. Eng.* **2018**, *6*, 1601-1612.
[5] M. Thomas and T. S. Natarajan, *Photocatalytic Nanomaterials for Environmental Applications* (Eds. R.J. Tayade, V. Gandhi), Materials Research Foundations, **2018**, vol. 27, pp. 48.
[6] R. Yadav, V. Amoli, J. Singh, M. K. Tripathi, P. Bhanja, A. Bhaumik and A. K. Sinha, *J. CO2 Util*. **2018**, *27*, 11-21.
[7] V. Amoli, M. G. Sibi, B. Banerjee, M. Anand, A. Maurya, S. A. Farooqui, A. Bhaumik and A. K. Sinha, *ACS Appl. Mater. Interfaces*. **2014**, *7*, 810-822.
[8] K. K. Paul and P. Giri, *J. Nanosci. Nanotechnol*. **2019**, *19*, 307-331.
[9] R. Hao, G. Wang, H. Tang, L. Sun, C. Xu and D. Han, *Appl. Catal.,B.* **2016**, *187*, 47-58.
[10] Y. Sui, C. Su, X. Yang, J. Hu and X. Lin, *J. Mol. Catal. A: Chem*. **2015**, *410*, 226-234.
[11] B. Li, X. Chen, T. Zhang, S. Jiang, G. Zhang, W. Wu and X. Ma, *Appl. Surf. Sci*. **2018**, *439*, 1047-1056.
[12] L. Lu, T. Jiang, W.-s. Jing, G.-w. Zhou and H.-x. Shi, *Chem. Lett.* **2018**, *47*, 613-616.
[13] X. Meng and Z. Zhang, *Mater. Lett.* **2018**, 225, 152-156.
[14] C.-C. Chen, J.-Y. Fu, J.-L. Chang, S.-T. Huang, T.-W. Yeh, J.-T. Hung, P.-H. Huang, F.-Y. Liu and L.-W. Chen, *J. Colloid Interface Sci.* **2018**, *532*, 375-386.
[15] D. Ni, W. Sun, L. Xie, Q. Fan, Z. Wang and K. Sun, *J. Power Sources*, **2018**, *374*, 166-174.

[16] S. Vadivel, B. Paul, D. Maruthamani, M. Kumaravel, T. Vijayaraghavan, S. Hariganesh and R. Pothu, *Mater. Sci. Energ. Technol*, **2019**, *2*, 112-116.
[17] J. Cheng, L. Frezet, P. Bonnet and C. Wang, *Catal. Lett.* **2018**, *148*, 1281-1288.
[18] A. V. Vorontsov and S. V. Tsybulya, *Ind. Eng. Chem. Res.* **2018**, *57*, 2526-2536.
[19] U. Holzwarth and N. Gibson, *Nat. Nanotechnol*. **2011**, *6*, 534.
[20] M. Nasr, L. Soussan, R. Viter, C. Eid, R. Habchi, P. Miele and M. Bechelany, *New J. Chem.* **2018**, *42*, 1250-1259.
[21] M. Salari, K. Konstantinov and H. K. Liu, *J. Mater. Chem.* **2011**, *21*, 5128-5133.
[22] A. J. Gmitter, A. Halajko, P. J. Sideris, S. G. Greenbaum and G. G. Amatucci, *Electrochim Acta*, **2013**, *88*, 735-744.
[23] C. Bittencourt, M. Rutar, P. Umek, A. Mrzel, K. Vozel, D. Arčon, K. Henzler, P. Krüger and P. Guttmann, *RSC Adv*. **2015**, *5*, 23350-23356.
[24] J. Han, G. Li, L. Qiang, X. Zhai and C. Jiang, *J. Mater. Sci. : Mater. Electron.* **2019**, *30*, 5995-6006.
[25] U. Diebold and T. Madey, *Surf. Sci. Spectra*, **1996**, *4*, 227-231.
[26] H.-P. Jiao, X. Yu, Z.-Q. Liu, P.-Y. Kuang and Y.-M. Zhang, *Rsc Adv.* **2015**, *5*, 16239-16249.
[27] A. Ghobadi, T. G. Ulusoy, R. Garifullin, M. O. Guler and A. K. Okyay, *Sci. Rep.* **2016**, *6*, 30587.
[28] X. Zhang and Z. Chen, *RSC Adv.* **2015**, *5*, 9482-9488.
[29] W. Su, J. Wang, Y. Huang, W. Wang, L. Wu, X. Wang and P. Liu, *Scr. Mater.* **2010**, *62*, 345-348.
[30] Y. G. Guo, Y. S. Hu, W. Sigle and J. Maier, *Adv. Mater.* **2007**, *19*, 2087-2091.
[31] J. Pan, Z. Dong, B. Wang, Z. Jiang, C. Zhao, J. Wang, C. Song, Y. Zheng and C. Li, *Appl. Catal. B: Environ.* **2019**, 242, 92-99.
[32] M. Nasr, R. Viter, C. Eid, R. Habchi, P. Miele and M. Bechelany, *Surf. Coat. Technol.* **2018**, *343*, 24-29.
[33] M. Canpolat, C. Kürkçü, Ç. Yamçıçıer and Z. Merdan, *Solid State Commun.* **2019**, *288*, 33-37.
[34] P. K. Sharma, M. A. L. Cortes, J. W. Hamilton, Y. Han, J. A. Byrne and M. Nolan, *Catal. Today,* **2019**, *321*, 9-17.
[35] Y. Yang, L. C. Yin, Y. Gong, P. Niu, J. Q. Wang, L. Gu, X. Chen, G. Liu, L. Wang and H. M. Cheng, *Adv. Mater.* **2018**, *30*, 1704479.
[36] H. Albetran, B. O'Connor and I. Low, *Mater. Des.* **2016**, *92*, 480-485.
[37] X.-j. Wang, Y. Zhao, F.-t. Li, L.-j. Dou, Y.-p. Li, J. Zhao and Y.-j. Hao, *Sci. Rep.* **2016**, *6*, 24918.
[38] H. Wei, W. A. McMaster, J. Z. Tan, D. Chen and R. A. Caruso, *J. Mater. Chem. A*, **2018**, *6*, 7236-7245.
[39] H. Yu, X. Quan, S. Chen and H. Zhao, *J. Phys. Chem. C*, **2007**, *111*, 12987-12991.
[40] Y. Zhang, J. Zhou, W. Cai, J. Zhou and Z. Li, *Applied Surface Science*, **2018**, *430*, 549-560.
[41] L. Sun, L. Xiang, X. Zhao, C.-J. Jia, J. Yang, Z. Jin, X. Cheng and W. Fan, *ACS Catal.* **2015**, *5*, 3540-3551.
[42] L. Sun, X. Zhao, C.-J. Jia, Y. Zhou, X. Cheng, P. Li, L. Liu and W. Fan, *J. Mater. Chem.* **2012**, *22*, 23428-23438.
[43] M. Yang, Q. Yang, J. Zhong, S. Huang, J. Li, J. Song and C. Burda, *Appl. Surf. Sci.* **2017**, *416*, 666-671.
[44] K. Kočí, K. Matějů, L. Obalová, S. Krejčíková, Z. Lacný, D. Plachá, L. Čapek, A. Hospodková and O. Šolcová, *Appl. Catal. B: Environ.* **2010**, *96*, 239-244.
[45] A.-W. Xu, Y. Gao and H.-Q. Liu, *J. Catal.* **2002**, *207*, 151-157.
[46] D. Ollis, *Appl. Catal. B: Environ.* **2019**, *242*, 431-440.
[47] M. Nasr, R. Viter, C. Eid, F. Warmont, R. Habchi, P. Miele and M. Bechelany, *RSC Adv.* **2016**, *6*, 103692-103699.
[48] X. Zhao, C. Yi, M. Zhang, C. Ma, C. Li and Y. Yan, *J. Nanosci. Nanotechnol.* **2018**, *18*, 4675-4683.
[49] M. Tasbihi, K. Kočí, M. Edelmannová, I. Troppova, M. Reli and R. Schomaecker, *J. Photochem. Photobiol. A: Chem.* **2018**, *366*, 72-80.
[50] B. Bukowski and N. A. Deskins, *Phys. Chem. Chem. Phys.* **2015**, *17*, 29734-29746.
[51] B. Bhanvase, T. Shende and S. Sonawane, *Environ. Technol. Rev.* **2017**, *6*, 1-14.

FULL PAPER

The novel BiOF/TiO_2 heterostructure with different molar ratio of BiOF and TiO_2 were successfully elaborated via simple solid state sintering method. The optimal molar ratio of BiOF/TiO_2 was found to be (1:3) with a photodegradation percentage of 91.2% and it was 7 and 5 times more efficient than that of pure BiOF or TiO_2 nanopowder, respectively.

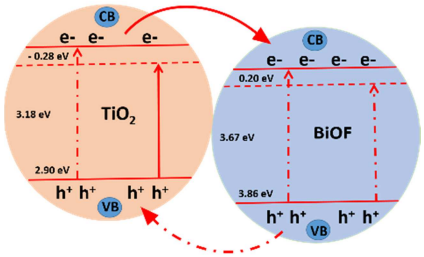

BiOF/TiO_2 heterostructure

Maryline Nasr, Wenshi Huang, Carla Bittencourt, Dandan Cui, Ying Sun, Lei Wang, Nathalie Gaillard Caperaa, Yuping Ning, Ping Song, Pierre Bonnet, and Cong Wang**

Page No. – Page No.

Synthesis of BiOF/TiO_2 heterostructures and their enhanced visible-light photocatalytic activity

FULL PAPER